communications biology

A Nature Portfolio journal

Article

https://doi.org/10.1038/s42003-025-07977-1

Targeting SCD triggers lipotoxicity of cancer cells and enhances anti-tumor immunity in breast cancer brain metastasis mouse models

Alessandro Sammarco[1,2,3] ✉, Giorgia Guerra[4], Katharina M. Eyme[1], Kelly Kennewick[2], Yu Qiao[2], Joelle El Hokayem[1], Kevin J. Williams[5,6], Baolong Su[5,6], Cagri Cakici[1], Hayk Mnatsakanyan[1], Valentina Zappulli[3], Steven J. Bensinger[2,5,7,8,10] & Christian E. Badr[1,9,10] ✉

Breast cancer brain metastases (BCBM) are incurable, and new therapies are urgently needed. BCBM upregulates stearoyl-CoA desaturase (SCD), an enzyme that catalyzes the synthesis of monounsaturated fatty acids, suggesting a potential metabolic vulnerability. Here, we test the effect of a brain-penetrant, clinical-stage SCD inhibitor (SCDi) on breast cancer cells and mouse models of BCBM. We show that SCDi markedly reshapes the lipidome of breast cancer cells, resulting in endoplasmic reticulum stress, DNA damage, impaired DNA damage repair, and cytotoxicity. Importantly, SCDi alone or combined with a PARP inhibitor prolongs the survival of BCBM-bearing mice. Furthermore, pharmacological inhibition of SCD enhances antigen presentation by dendritic cells, increases interferon signaling, promotes the infiltration of cytotoxic T cells, and decreases the proportion of exhausted T cells and regulatory T cells (Tregs) in the tumor microenvironment (TME) in a syngeneic mouse model of BCBM. Additionally, SCDi reduces the engagement of immunosuppressive pathways, including the PD-1:PD-L1/PD-L2 and PVR/TIGIT axes in the TME. These findings suggest that SCD inhibition could be an effective strategy to both intrinsically reduce tumor growth and reprogram anti-tumor immunity in the brain microenvironment to treat BCBM.

Approximately 20% of cancer patients develop brain metastases (BM), the majority of which result from lung (20–56%), breast (5–20%), melanoma (7–16%), kidney (4–11%), and colorectal cancer (1–12%)[1–6]. Despite multimodal therapies, including surgical resection, chemotherapy, radiotherapy, and immunotherapy, individuals with BM have a poor prognosis, with an overall 2-year survival below 10%[1,7]. Therefore, novel and effective therapies for patients with BM are urgently needed.

Increasing evidence suggests that the brain microenvironment forces metastatic cells to undergo lipid metabolic adaptations to survive and proliferate in the brain. Metabolic rewiring highlights potential vulnerabilities that can be exploited to develop targeted therapies. For example, it has been shown that considerably lower levels of triacylglycerols (TAGs) are available in the brain than in the tissue environment of the primary tumor. As a result, metastatic cells must synthesize requisite lipids de novo to meet the anabolic demands of proliferation[8]. In support of this idea, BM from human breast cancer (HBC) upregulates several enzymes involved in fatty acid synthesis and metabolism, including stearoyl-CoA desaturase (SCD)[9]. This key enzyme converts saturated fatty acids (SFAs) into monounsaturated fatty acids (MUFAs)[8,9]. The balance between SFAs and MUFAs contributes to the biophysical properties of cell membranes,

[1]Department of Neurology, Massachusetts General Hospital, Boston, MA, USA. [2]Department of Microbiology, Immunology, and Molecular Genetics, University of California, Los Angeles, Los Angeles, CA, USA. [3]Department of Comparative Biomedicine and Food Science, University of Padua, Padua, Italy. [4]Graduate School of Biomedical Sciences, Cedars-Sinai Medical Center, Los Angeles, CA, USA. [5]UCLA Lipidomics Lab, University of California, Los Angeles, Los Angeles, CA, USA. [6]Department of Biological Chemistry, University of California, Los Angeles, Los Angeles, CA, USA. [7]Department of Molecular and Medical Pharmacology, University of California, Los Angeles, Los Angeles, CA, USA. [8]Jonsson Comprehensive Cancer Center, David Geffen School of Medicine, University of California, Los Angeles, Los Angeles, CA, USA. [9]Neuroscience Program, Harvard Medical School, Boston, MA, USA. [10]These authors jointly supervised this work: Steven J. Bensinger, Christian E. Badr. ✉e-mail: alessandro.sammarco6@gmail.com; badr.christian@mgh.harvard.edu

such as fluidity, permeability, and the spatial assembly of membrane properties[10]. SCD also regulates the pool of MUFAs, which serve as building blocks for more complex lipids (e.g., phospholipids and TAGs) that are critical for cell survival[10]. The heightened expression of SCD and an increased reliance on de novo synthesis of MUFAs in breast cancer brain metastases (BCBM) has led to the hypothesis that this metabolic enzyme could be an attractive therapeutic target in metastatic disease. However, SCD inhibitors (SCDis) (e.g., CAY10566, A939572, and MF-438) have a limited capacity to cross the BBB, hampering their clinical relevance for BM. Recently, a novel brain-penetrant SCDi, YTX-7739, has been identified as a lead clinical candidate for treating synucleinopathies[11]. The pharmacokinetic and pharmacodynamic properties of YTX-7739 have been extensively investigated in multiple preclinical species[11]. These data demonstrated its preclinical safety and ability to penetrate the BBB, making it a suitable candidate for the treatment of brain malignancies. In our previous work, we showed that SCD is also essential for glioblastoma (GBM) tumor growth[12], and demonstrated the therapeutic efficacy of this SCDi in GBM mouse models[13].

Another important factor underlying the growth and survival of brain metastatic tumors is their interaction with the immune system. Several immune subsets exist within the brain tumor microenvironment (TME) that can have distinct and sometimes opposing roles. Increasing evidence suggests that fatty acid homeostasis in immune cells represents a key regulatory node to control inflammation, and manipulation of fatty acid metabolism has significant effects on immune cell functions[14–16]. While the efficacy of pharmacological inhibition of SCD was already investigated in extracranial tumors and GBM[13,17,18], its effect on cancer cells and anti-tumor immunity in the BCBM TME has not been examined. Therefore, we studied the effect of YTX-7739 in BCBM and examined the impact of pharmacological inhibition of SCD at the single-cell level on cancer and immune cells in the TME.

Results

SCD inhibition reshapes the lipid composition of breast cancer cells

To confirm the on-target effect and evaluate the influence of YTX-7739 (hereafter referred to as SCDi) on fatty acid synthesis flux in our model, triple-negative breast cancer (TNBC) cells HCC1806 and MDA-MB-468 were cultured in ^{13}C-glucose-containing media and treated with SCDi at different doses. After 24 h and 48 h of labeling/treatment, lipids were extracted and analyzed by GC-MS to determine isotope enrichment into long-chain fatty acids. Isotopologues were then modeled using isotope spectral analysis (ISA) to assess the contribution of synthesis to the total cellular fatty acid pool in the cells. As expected, pharmacological inhibition of SCD led to a significant dose- and time-dependent increase of synthesized SFA 18:0, an SCD substrate, and a corresponding decrease in SCD products 16:1 and 18:1 (Figs. 1A and S1A, B). Accordingly, the fatty acid desaturation index (FADI), which measures SCD activity, was significantly reduced in cells treated with SCDi (Figs. 1A and S1B), consistent with our previous work[12,13], confirming its on-target effect in TNBC cells. To determine the influence of pharmacological inhibition of SCD on the lipidome of TNBC cells in greater depth, we performed shotgun lipidomics on brain-tropic MDA-MB-231-BR (hereinafter referred to as MDA-BR) treated with SCDi (1 μM) for 48 h. Approximately 900 individual lipid species from 17 lipid subclasses were measured. Cluster analysis of individual lipid species revealed that SCDi treatment markedly changed the lipid composition of MDA-BR cells (Figs. 1B and S1C–E). Analysis of SFAs and MUFAs incorporation into phospholipids (PLs), triacylglycerides (TAGs), and cholesteryl esters (CEs) revealed that SCDi treatment showed an increased proportion of SFAs, and a corresponding decreased proportion of MUFAs, consistent with SCD inhibition (Figs. 1C and S1F). Of note, the difference in SFAs between control and SCDi was much higher in TAGs (47% vs 73%, respectively) and in CEs (33% vs 57%, respectively), compared to PLs (38% vs 43%, respectively). Interestingly, in SCDi-treated cells, the percentage of polyunsaturated fatty acids (PUFAs) increased only in PLs, while decreasing in TAGs and CEs (Fig. 1C). Together, these data confirm that SCDi inhibits SCD-dependent MUFA synthesis and can markedly reshape the breast cancer cell lipidome.

Pharmacologic inhibition of SCD induces apoptosis, triggers ER stress, and is associated with DNA damage

Next, we evaluated the functional consequences of pharmacological inhibition of SCD on HBC cells. First, we assessed the viability and mechanism of cell death of HBC cells treated with different doses of SCDi. SCDi decreased the viability of HBC cells in a dose-dependent manner (Figs. 1D and S2A, B), mainly via apoptosis (Figs. 1E and S2C, D). Notably, the TNBC cell lines MDA-MB-231, MDA-BR, HCC1806, and MDA-MB-468 were the most sensitive to SCDi (Fig. S2A), suggesting a high efficacy of SCDi on aggressive HBC cells in vitro. It is known that the accumulation of SFAs leads to lipotoxicity, which activates the endoplasmic reticulum (ER) stress response[19]. Consistent with lipotoxicity, we observed a time-dependent increase of ER stress in HBC cells when cells were treated with SCDi (Figs. 1F and S2E, F). As expected, supplementing cell cultures with 18:1, the major product of SCD, rescued HBC cells from SCDi-induced cell death (Fig. S2G). These data confirm the critical role of SCD-mediated desaturation in regulating lipotoxicity and influencing cell survival and proliferation.

Recent work from our lab and others has shown a link between DNA damage and inhibition of fatty acid synthesis in cancer cells[13,20]. Therefore, to further investigate the mechanism of SCDi-induced cell death in our model, we treated HBC cells with SCDi (1 μM) and evaluated DNA damage and repair pathways at different timepoints. DNA double-strand breaks are typically repaired by two major mechanisms: non-homologous end joining (NHEJ) and homology-directed repair (HDR), the latter being mediated by RAD51. Consistent with our published work[12,13], pharmacological inhibition of SCD increased the expression of DNA damage marker γ-H2AX and decreased the expression of RAD51 in HBC cells, particularly after 48/72 h of treatment (Figs. 1G and S2H). Interestingly, when MDA-BR were treated with SCDi (1 μM) and the pan-caspase inhibitor Z-VAD-FMK (50 μM), which significantly reduced apoptosis (Fig. S2I), the protein expression of γ-H2AX was decreased (Fig. S2J), suggesting that DNA damage was caused primarily by engagement of apoptosis. However, SCDi-induced down-regulation of RAD51 was independent of apoptosis (Fig. S2J), suggesting a direct link between inhibition of SCD and DNA damage repair (DDR) deficiency. Then, we hypothesized that ER stress was upstream of the induction of DNA damage. Therefore, we treated HBC cells with SCDi with or without ER stress inhibitors for 48 h. In line with our hypothesis, we found that when ER stress was inhibited (particularly with the PERK inhibitor GSK2606414), SCDi-induced γ-H2AX increased expression was significantly attenuated, suggesting that ER stress might be upstream of the induction of DNA damage (Fig. S2L).

Next, we functionally measured DDR upon SCD inhibition using our established bioluminescent repair reporter (BLRR)[21], whereby BLRR-expressing cells secrete either Gaussia luciferase (GLuc) when DNA damage is repaired by HDR or Vargula luciferase (VLuc) when DNA damage is repaired through NHEJ (Fig. S2K). We treated BLRR-expressing MDA-BR cells with different doses of SCDi and measured GLuc and VLuc activities in the cell culture medium over time. As expected, SCDi decreased the ratio HDR/NHEJ in a dose- and time-dependent manner, consistent with a down-regulation of RAD51 (Figs. 1H and S2K). To explore whether SCDi similarly decreased HDR in breast tumors in vivo, we implanted BLRR-expressing MDA-BR cells into the mammary fat pad of mice, and, upon tumor engraftment, we treated them with SCDi (50 mg/kg) for 21 days. Then, we measured GLuc and VLuc activity in the blood and confirmed a decreased HDR/NHEJ ratio in mice treated with SCDi (Fig. 1I). Together, these data show that SCDi triggers ER stress, induces DNA damage, and hinders DDR by inhibiting HDR in TNBC cells. They also support the idea that SCDi-mediated DDR blockade/HDR deficiency could be an exploitable vulnerability for cancer cells.

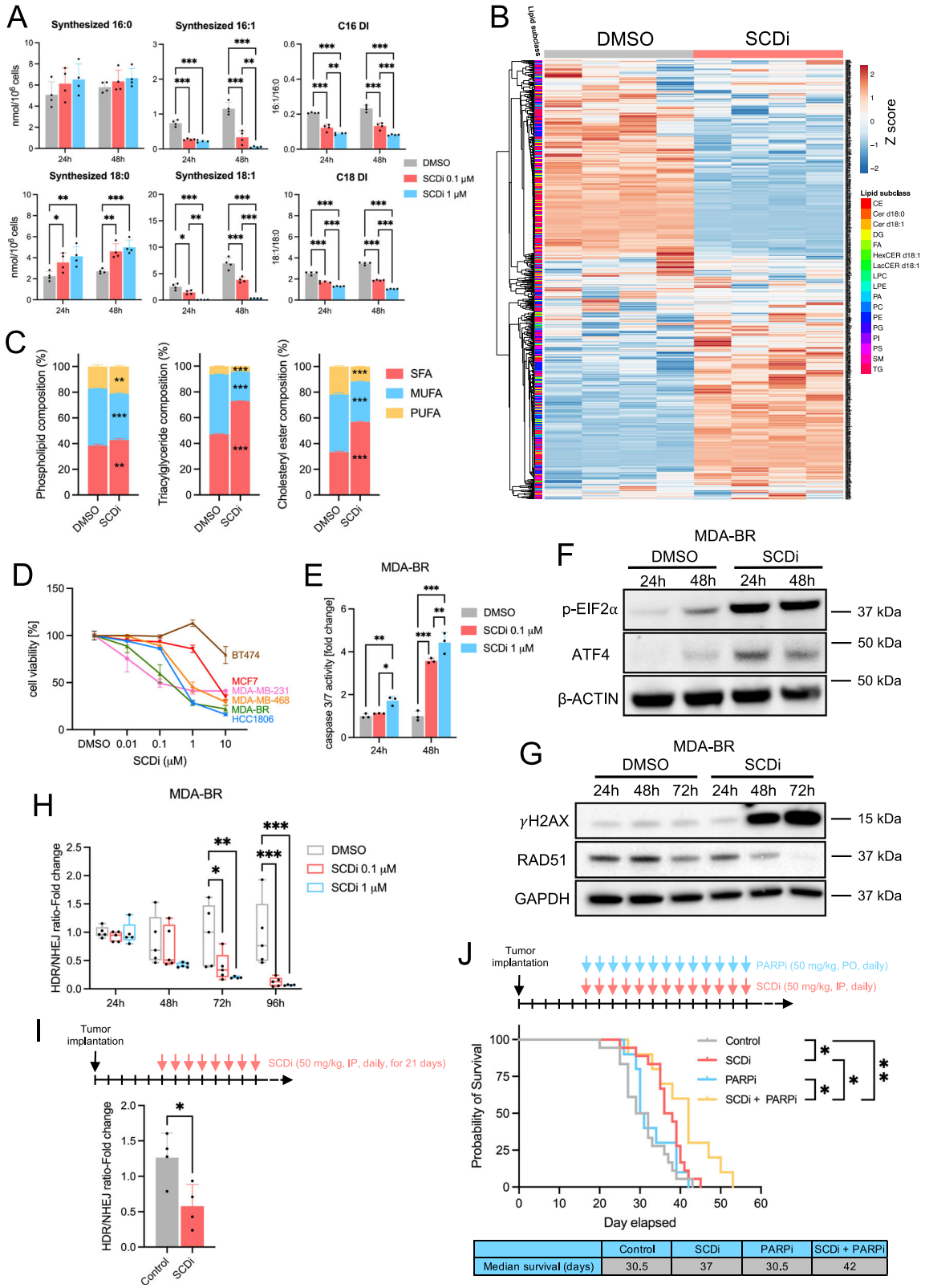

	Control	SCDi	PARPi	SCDi + PARPi
Median survival (days)	30.5	37	30.5	42

Treatment with SCDi and a PARP inhibitor prolongs survival in a mouse model of BCBM

It is known that poly(ADP-ribose) polymerase (PARP) inhibitors (PARPi), which exert an anti-tumor effect by inhibiting the repair of DNA single-strand breaks[20], are particularly effective against cancer cells with HDR deficiency[22–24], such as breast cancer cells defective for BRCA1/2[25], while showing lower efficacy in BRCA1/2 wild-type tumors[26]. Because of this, PARPi has shown potential in treating BCBM, particularly in patients with BRCA1/2 mutations[27]. Therefore, we hypothesized that impaired HDR following SCD inhibition would sensitize HBC cells to PARPi. We tested this hypothesis using a BRCA1 wild-type, PARPi-resistant MDA-BR BCBM mouse model[26]. To model breast cancer metastasis to the brain, we opted for

Fig. 1 | Inhibition of SCD induces ER stress, is associated with DNA damage, and prolongs survival in a mouse model of BCBM. A Gas chromatography/mass spectrometry of HCC1806 treated with SCDi (0.1 μM or 1 μM) for 24 h or 48 h, measuring synthesized palmitic acid (16:0), palmitoleic acid (16:1), stearic acid (18:0), and oleic acid (18:1). On the right, the desaturation index (DI—ratio 16:1/16:0 and 18:1/18:0) is shown. Each data point represents a biological replicate ($n = 4$). Mean ± SD (two-way ANOVA, Tukey's test). **B** Heat map of all individual lipids quantified using shotgun lipidomics of MDA-BR treated with SCDi (1 μM) for 48 h. CE cholesteryl esters, Cer ceramides, DG diacylglycerols, FA free fatty acids, HexCER hexosylceramides, LacCER lactosylceramides, LPC lysophosphatidylcholines, LPE lysophosphatidylethanolamines, PA phosphatidic acid, PC phosphatidylcholines, PE phosphatidylethanolamines, PG phosphatidylglycerols, PI phosphatidylinositol, PS phosphatidylserines, SM sphingomyelin, TG triacylglycerols. Each column represents a biological replicate ($n = 4$). **C** Stacked histograms showing SFAs, monounsaturated FAs (MUFAs), and polyunsaturated FAs (PUFAs) composition in phospholipids, triacyglicerides, and cholesteryl esters of MDA-BR treated with SCDi (1 μM) for 48 h, measured by shotgun lipidomics ($n = 4$). Mean ± SD (Student's *t*-test). Statistics refers to DMSO vs SCDi. **D** Cell viability of breast cancer cells treated with different doses of SCDi for 72 h ($n = 3$). Mean ± SD. **E** Caspase 3/7 assay of MDA-BR treated with SCDi (0.1 μM or 1 μM) for 24 h or 48 h. Each data point represents a biological replicate ($n = 3$). Mean ± SD (two-way ANOVA, Tukey's test). **F**, **G** Western blot for (**F**) ER stress and (**G**) DNA damage markers in MDA-BR treated with SCDi (1 μM) for 24 h, 48 h, or 72 h. Representative data from three biological replicates. **H**, **I** Vargula luciferase (Vluc) and Gaussia luciferase (Gluc) assay measured as fold change in HDR/NHEJ in (**H**) BLRR-expressing MDA-BR treated with SCDi (0.1 μM or 1 μM) for 24 h, 48 h, 72 h, or 96 h in vitro and **I** plasma of mice subcutaneously implanted with BLRR-expressing MDA-BR and treated with vehicle ($n = 4$) or SCDi (50 mg/kg; $n = 4$) for 21 days. **H** Each data point represents a biological replicate ($n = 5$). Mean ± SEM (two-way ANOVA, Tukey's test). **I** Each data point represents the average of three technical replicates for each mouse ($n = 4$). Mean ± SD (Student's *t*-test). **J** Overall survival of mice implanted with MDA-BR intracranially and treated with either vehicle ($n = 18$), SCDi (50 mg/kg; $n = 18$), PARPi (50 mg/kg; $n = 10$), or SCDi (50 mg/kg) + PARPi (50 mg/kg) ($n = 10$). Log-rank (Mantel–Cox) test was performed per each pair of groups. $^{*}p < 0.05$; $^{**}p < 0.01$; $^{***}p < 0.001$.

the direct implantation of MDA-BR in the brains of mice, as shown by other authors[26,28–30]. Five days following intracranial implantation, mice were treated with SCDi alone (50 mg/kg, IP, daily) or in combination with the brain-penetrant PARPi Niraparib (50 mg/kg, PO, daily). SCDi treatment alone led to a significant increase in overall survival (median survival 37 days for SCDi vs 30.5 days for control; $p = 0.0138$), suggesting the efficacy of SCDi for treating BCBM. As expected, PARPi alone had no therapeutic effect ($p = 0.531$). However, combining SCDi with PARPi further enhanced the overall survival of BCBM-bearing mice (median survival 42 days for SCDi + PARPi vs 30.5 days for control; $p = 0.0017$) (Fig. 1J). These data demonstrate a direct effect of SCDi on cancer cells in vivo, underscoring its therapeutic efficacy in a BCBM mouse model and supporting further investigation of rational combinations of SCD and PARP inhibitors for treating BCBM.

Effect of pharmacological inhibition of SCD in a syngeneic mouse model of BCBM

The balance of SFAs and MUFAs, tightly regulated by SCD activity, is an important regulator of the inflammatory responses in immune cells[31,32]. Therefore, we asked whether pharmacological inhibition of SCD would affect the anti-tumor immune response in a syngeneic mouse model of BCBM. First, we studied the effects of SCD inhibition in the mouse mammary cancer cell line EO771 in vitro. As expected, SCDi caused cytotoxicity (Fig. S3A), which was rescued by oleic acid 18:1 (Fig. S3B), reduced the FADI (Fig. S3C), and triggered ER stress (Fig. S3D) in the EO771 cells. These data confirm that SCDi had the same effects on human and murine mammary cancer cells. Next, immunocompetent C57BL/6 mice were intracranially implanted with EO771 cells. Starting at day 4 after implantation, mice received daily doses of vehicle (Control; $n = 8$) or SCDi (50 mg/kg, IP; $n = 8$) for 14 days (Fig. 2A). Tumor volume was significantly decreased in mice treated with SCDi (Fig. 2B). On the day of euthanasia, brain tumors from three representative mice per group were dissociated, and tumor and immune cells were sorted and submitted for single-cell RNA sequencing (scRNAseq) (Fig. 2A). Of note, SCDi-treated tumors showed a higher immune cell/tumor cell ratio when compared to the control (61.2%/29% and 55.6%/33.4%, respectively), reflective of a lower number of tumor cells in SCDi-treated tumors (Fig. S4).

Tumor cells were clustered based on DEGs and visualized using a uniform manifold approximation and projection (UMAP) plot, which identified three main tumor cell subclusters (Fig. 2C). Due to non-specific gene signatures characterizing these subclusters and to their similar proportions between the treatment groups (Fig. 2D), we proceeded with the analysis considering all clusters together. We analyzed DEGs in tumor cells between control and SCDi-treated tumors and performed pathway analysis. This analysis revealed a significant dysregulation of the G2/M checkpoint, E2F targets, and DNA repair pathways (Fig. 2E), with most of the genes belonging to the G2/M checkpoint pathway being upregulated in SCDi-treated tumors (Fig. 2F). These pathways are activated following DNA damage[33,34]. Therefore, dysregulation of these pathways is likely caused by DNA damage upon SCD inhibition, which is in line with previous data on impaired HDR and elevated DNA damage following treatment with SCDi (Figs. 1G-I and S2H). The TGF-beta signaling pathway was also significantly altered (Fig. 2E), with most of the genes (e.g., *Wwtr1*, *Smurf1*, *Serpine1*, and *Tgfbr1*) down-regulated in SCDi-treated tumors (Fig. 2F), which could indicate down-regulation of this pathway upon SCD inhibition. This pathway plays a key role in cancer progression, and its inhibition is associated with a better outcome[35]. Lastly, TNF-alpha signaling via NF-kB was also significantly dysregulated (Fig. 2E), with most of the genes (e.g., *Nfat5*, *B4galt1*, *Areg*, *Ccn1*, and *Ier3*) downregulated in SCDi-treated tumors (Fig. 2F). Conversely, NF-kB inhibitors *Nfkbia* and *Nfkbie* were upregulated with SCD inhibition, suggesting inhibition of this pathway, as previously shown in ovarian cancer[36]. Together, these data confirm DDR inhibition and suggest the downregulation of two key pathways involved in tumor progression in SCDi-treated tumors.

Pharmacological inhibition of SCD enhances antigen presentation and interferon signaling of dendritic cells (DCs)

Unsupervised clustering of $CD45^{+}$ cells based on DEGs identified 10 main cell types, including macrophages, monocytes, DCs, T cells, natural killer (NK) cells, Tregs, B cells, plasmacytoid dendritic cells (pDCs), microglia, and neutrophils (Fig. 2G, H). Interestingly, pharmacological inhibition of SCD was associated with alterations to the tumor immune cell landscape. Particularly, tumors treated with SCDi showed enrichment of monocytes (+21%) and macrophages (+11%), and a decreased percentage of DCs (−31%) and Tregs (−49%), when compared to vehicle-treated tumors (Fig. 2I).

Next, we analyzed individual immune cell populations, starting with DCs, given their importance in antigen presentation and anti-tumor immunity[37]. Cluster analysis of DCs identified two main sub-clusters: mature DCs enriched in immunomodulatory molecules (mregDCs), expressing *Fscn1*, *Mreg*, *Ccr7*, *Stat4*, *Cd200*, *Samsn1*, and *Socs2*, and pro-inflammatory antigen-presenting DCs (AP-DCs), expressing *H2-DMb1*, *H2-DMa*, *H2-Ab1*, *Fcer1g*, *Ifitm6*, and *Cd209a* (Fig. 3A, B). MregDCs were recently identified as a novel DC subpopulation in the TME with both immunostimulatory and immunosuppressive functions[38]. Compositional analysis revealed a decrease in the percentage of mregDCs and an increase in the percentage of AP-DCs (Fig. 3C). Based on this, we hypothesized that DCs from SCDi-treated tumors had an enhanced antigen-presenting capacity. Therefore, we analyzed DEGs in DCs between vehicle- and SCDi-treated tumors and performed a pathway analysis that revealed enrichment of the antigen processing and presentation pathway (Fig. 3D). In line with our hypothesis, DCs from SCDi-treated tumors showed an upregulation of

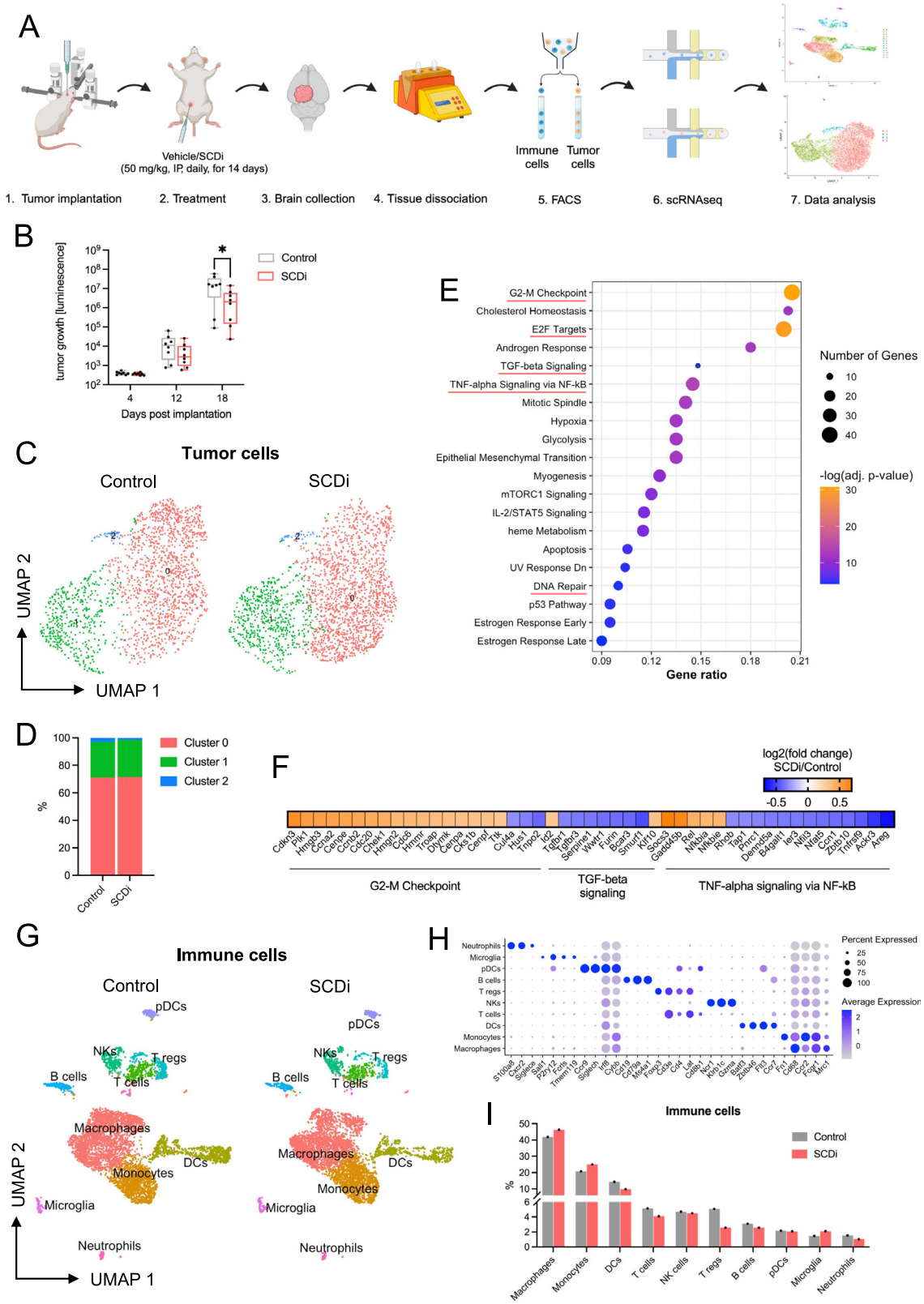

Fig. 2 | Pharmacological inhibition of SCD remodels the immune cell composition of the TME. A Schematic of treatment and tissue processing for single cell RNA sequencing (scRNAseq) in a syngeneic mouse model of breast cancer brain metastasis (BCBM). FACS, fluorescent-activated cell sorting. This schematic was created with BioRender.com **B** Luciferase assay from blood collected over time from BCBM-bearing mice treated with vehicle (control; $n = 8$) or SCDi (50 mg/kg; $n = 8$) to measure tumor volume. **C** Uniform manifold approximation and projection (UMAP) of tumor cells in BCBM treated with control ($n = 3$) and SCDi ($n = 3$). **D** Histogram showing proportions of tumor cell subclusters in control and SCDi-treated tumors. **E** Pathway analysis (MSigDB) of differentially expressed genes (DEGs) in tumor cells (SCDi vs control). **F** Heatmap representing DEGs belonging to G2-M checkpoint, TGF-beta signaling, and TNF-alpha signaling via NF-kB pathways in control and SCDi-treated tumors. **G** UMAP of immune cells in control and SCDi-treated tumors. **H** Dot plot of average expression of canonical marker genes for the main immune cell subtypes. **I** Histogram showing cell frequency of immune cells in control and SCDi-treated tumors. $^{*}p < 0.05$.

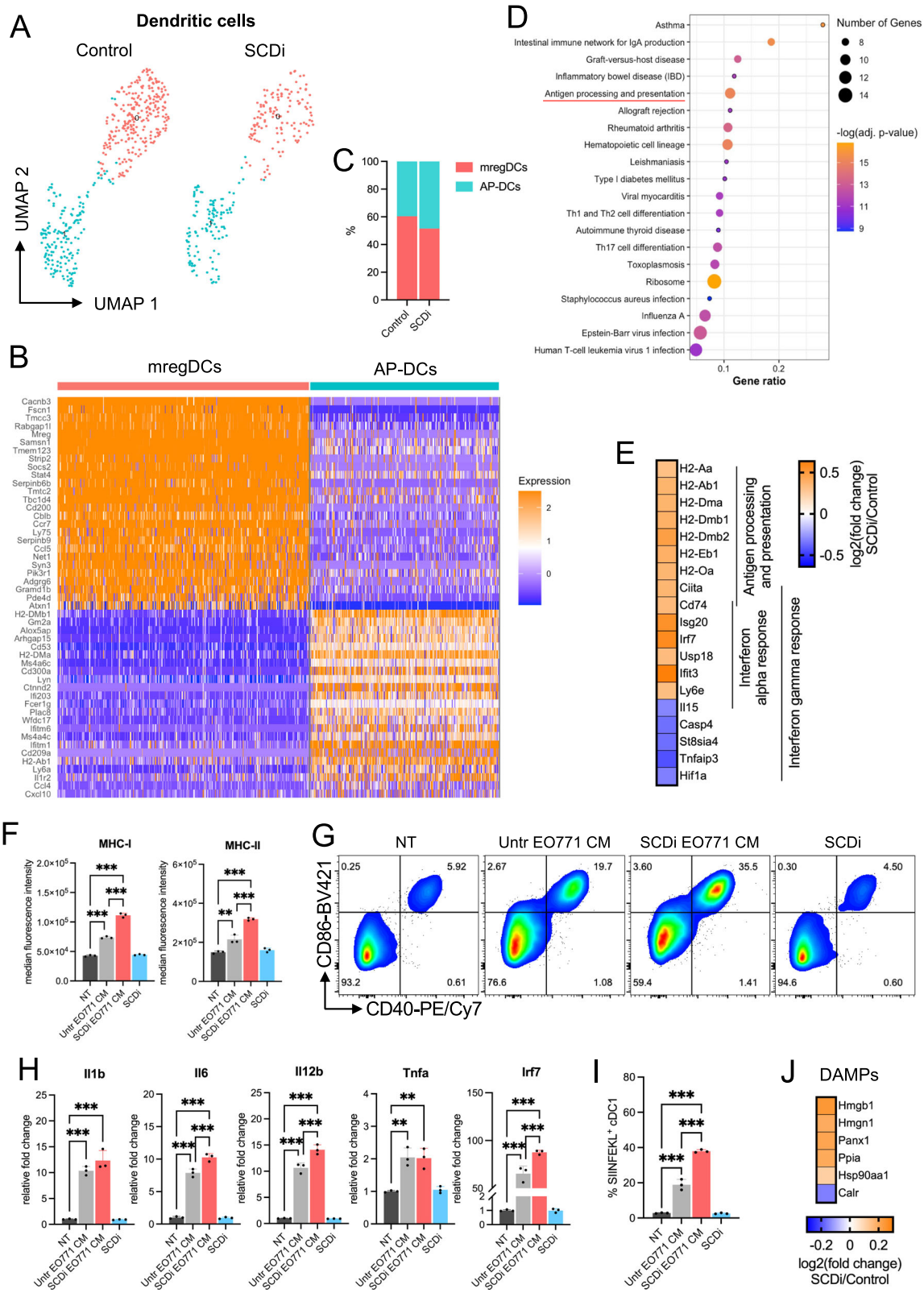

genes encoding the MHC-II protein subunits (*H2-Aa*, *H2-Ab1*, *H2-DMa*, *H2-DMb1*, *H2-DMb2*, *H2-Eb1*, and *H2-Oa*), the invariant chain *Cd74*, a polypeptide that plays a critical role in antigen presentation, facilitating the transport of MHC-II from the ER to the cell surface, and *Ciita*, a master controller of antigen presentation (Fig. 3E). Thus, these data suggest that pharmacological inhibition of SCD is associated with an enhanced antigen presentation capacity of DCs in the TME, which might indicate a better anti-tumor response. Moreover, pathway analysis showed a significant dysregulation of pathways related to interferon alpha, interferon gamma, and the inflammatory response (Fig. S5A). Interestingly, when we analyzed the expression of genes belonging to these pathways, we found that interferon genes *Isg20*, *Irf7*, and *Ifit3* were upregulated in SCDi-treated tumors

Fig. 3 | Antigen presentation and interferon signaling of DCs are enhanced in response to pharmacological inhibition of SCD. A UMAP of DCs in control and SCDi-treated tumors. **B** Heatmap of the top 20 upregulated genes in the dendritic cell subclusters. mregDCs, mature DCs enriched in immunomodulatory molecules; AP-DCs antigen-presenting DCs. **C** Histograms representing proportions of dendritic cell subpopulations in control and SCDi-treated tumors (relative to DCs). **D** Pathway analysis (KEGG) of the differentially expressed genes (DEGs) in DCs (SCDi vs control). **E** Heatmap representing DEGs belonging to antigen presentation and processing, interferon alpha, and interferon gamma response pathways in DCs (SCDi vs control). **F** Histograms representing median fluorescence intensity of MHC-I and MHC-II measured by flow cytometry, **G** scatterplot representing the expression of CD40 and CD80 measured by flow cytometry, **H** histograms representing relative fold change of *Il1b*, *Il6*, *Il12b*, *Tnfa*, and *Irf7* measured by qPCR, and **I** histograms representing the expression of SIINFEKL+ type I conventional dendritic cells (cDC1s) that were either not treated (NT), exposed to DMSO-treated (Untr) EO771 conditioned medium (CM), to SCDi-treated (SCDi) EO771 CM, or to SCDi alone for 24 h. Each data point represents a biological replicate ($n = 3$). Mean ± SD (two-way ANOVA, Tukey's test). $^{**}p < 0.01$; $^{***}p < 0.001$. **J** Heatmap representing the gene expression of damage-associated molecular patterns (DAMPs) in tumor cells (SCDi vs control).

compared to the control (Fig. 3E), suggesting a higher interferon signaling in DCs upon SCD inhibition.

To validate these results, we generated type I conventional dendritic cells (cDC1s) from murine bone marrow cells in vitro (Fig. S5B, C). Then, we exposed terminally differentiated cDC1s to DMSO- or SCDi-treated EO771 conditioned medium (CM) and assessed their activation status by flow cytometry and qPCR. Remarkably, the expression of MHC-I, MHC-II (signal I) (Fig. 3F), CD40, CD80, CD86 (signal 2) (Figs. 3G and S5D) and *Il1b*, *Il6*, *Il12b*, *Tnfa*, and *Irf7* (signal 3) (Fig. 3H) were significantly increased in cDC1s exposed to SCDi-treated EO771 CM, when compared to DMSO-treated (Untr) EO771 CM, suggestive of a higher activation status. Next, we employed the ovalbumin model to examine antigen presentation further. Briefly, after culture with EO771 CM, cDC1s were pulsed with the ovalbumin K^b-binding peptide SIINFEKL for 1 h. Staining for $OVA_{257\text{-}264}$ peptide (SIINFEKL) loaded onto MHC-I protein showed that stimulation with SCDi-treated EO771 CM increased antigen presentation in cDC1s (Figs. 3I and S5E). These data may suggest that pharmacological inhibition of SCD induces the release of molecules from cancer cells that function as damage-associated molecular patterns (DAMPs), known to activate immune cells, such as DCs[39]. This led us to ask if inhibition of SCD was associated with a higher expression of DAMPs in vivo. Therefore, we used our scRNAseq data and examined the expression of DAMPs in tumor cells in BCBM. In line with our hypothesis, the expression of several DAMPs (e.g., *Hmgb1, Hmgn1, Panx1, Ppia*, and *Hsp90aa1*) was higher in SCDi-treated tumors when compared to the control (Fig. 3J). Together, these data suggest that pharmacological inhibition of SCD is associated with enhanced antigen presentation, activation, and interferon signaling in DCs, as well as increased expression of DAMPs in tumor cells within the TME.

Macrophages from SCDi-treated tumors show higher pro-inflammatory activity

Re-clustering of macrophages identified 3 subpopulations (Fig. 4A). Analysis of the top 30 highly expressed genes for each subcluster revealed that macrophage subpopulation 0 expressed genes associated with antigen presentation (*H2-Eb1*, *H2-Ab1*, *H2-Aa*, *H2-DMb1*, *H2-DMa*, and *Cd74)*, and with a pro-inflammatory/anti-tumor M1 phenotype (*Il-1β* and *Cxcl9*). Macrophage subpopulation 1 highly expressed *Folr2*, a gene that has been associated with $CD8^+$ T cell infiltration and favorable prognosis in HBC[40], and many cytokines (*Ccl2*, *Ccl4*, *Ccl6*, *Ccl7*, *Ccl8*, *Ccl9*, *Cxcl10*). Macrophage subpopulation 2 expressed genes not indicative of a specific status (Fig. 4B). Compositional analysis revealed an increase of *Folr2*$^+$/cytokines-expressing macrophages in SCDi-treated tumors (Fig. 4C). Next, we analyzed the DEGs between vehicle- and SCDi-treated macrophages. We performed a pathway analysis, which revealed an enrichment of pathways associated with interferon alpha, interferon gamma, and inflammatory response (Fig. 4D). The majority of DEGs belonging to these pathways (e.g., *Ifitm3*, *Isg20*, *Psme1*, *Irf7*, *Isg15*, *Gbp2*, *Ifit3*, *Ccl7*, and *Fgl2*) were upregulated in macrophages from SCDi-treated tumors (Fig. 4E), indicating higher interferon signaling in these tumors. These data suggest an enhanced pro-inflammatory/anti-tumor activity of macrophages upon pharmacological inhibition of SCD.

Pharmacological inhibition of SCD triggers anti-tumor T cell responses in the TME

Next, we analyzed the T cell gene expression programs in response to SCDi. Unsupervised clustering of T cells identified 4 main subpopulations: activated cytotoxic T cells (*CD3e*, *CD8a*, *Cd8b1*, *Gzmb*, *Nkg7*, *Prf1*, *Cd69*, and *Cd28*), a subpopulation composed of T cells (*Cd3e*) and contaminating macrophages (*Adgre1, Fcgr1, Cd68*) that we named T cells + macrophages, activated T helper cells (*Cd3e, Cd4, Cd69, Cd28*), and exhausted T helper cells (*Cd3e*, *Cd4*, *Pdcd1*, *Tigit*, *Ctla4*, *Tnfrsf9*, *Havcr2*, and *Lag3*) (Fig. 4F, G). Compositional analysis revealed a higher proportion of activated cytotoxic T cells and a lower proportion of exhausted T helper cells in SCDi-treated tumors compared to the control (Fig. 4H), which could indicate a more efficient anti-tumor T cell response. Pathway analysis of the DEGs between control- and SCDi-treated tumors showed significant enrichment of interferon alpha, interferon gamma, and inflammatory response pathways (Fig. 4I). Analysis of specific gene signatures showed an upregulation of many interferon genes (e.g., *Ifit1*, *Ifit2*, *Ifit3*, *Isg20*, and *Irf7*), chemokines (*Xcl1* and *Ccl5*) known to play an important role in T cell activation and DC recruitment in the TME[41], and *Gzmb*, a potent cytotoxic protease used by cytotoxic T cells to kill cancer cells, in SCDi-treated tumors compared to the control (Fig. 4J). We also observed the downregulation of *Ccl8* in SCDi-treated tumors. Since Ccl8 is associated with Treg recruitment[42], this provide additional evidence for the reduced presence of intratumoral Tregs upon SCD inhibition, as shown by compositional analysis of immune cell populations (Fig. 2I). Pharmacological inhibition of SCD also decreased the expression of *Lag3* and *Ctla4*, which are associated with T cell exhaustion (Fig. 4J). Taken together, these data suggest that SCDi induces a higher interferon response in T cells and decreases the immunosuppressive effects of Tregs and exhausted T cells to support anti-tumor T cell responses.

CellChat analysis shows stronger interactions via MHC-I and weaker immunosuppressive PD-1:PD-L1/PD-L2 and PVR/TIGIT axes interactions upon SCD inhibition

The transcriptomic changes in immune cells in response to pharmacological inhibition of SCD led us to perform cell-to-cell interaction analysis across all immune cell subpopulations using CellChat. Initially, we examined the signaling pathways of all receptor-ligand interactions between the immune cell populations (Fig. 5A). SCDi-treated tumors showed stronger interactions (thicker lines) between all APCs (AP-DCs, mregDCs, monocytes, macrophages, neutrophils, microglia, pDCs, and B cells) and T/NK cells via MHC-I (Figs. 5B and S6A), consistent with higher antigen presentation through MHC-I when SCD is inhibited, in line with our functional DC studies (Fig. 3F). Additionally, SCDi-treated tumors showed similar interactions between APCs (AP-DCs, macrophages, and B cells) and T cells via MHC-II (Figs. 5C and S6B). Moreover, in line with our pathway analyses, CellChat showed weaker interactions (thinner lines) via PD-L1/PD-L2 immune checkpoints (Figs. 5D–E and S6C, D) and PVR/TIGIT (Figs. 5F, G and S6E, F) in SCDi-treated tumors. The latter is an immunosuppressive axis that leads to an anti-inflammatory, non-proliferative, non-cytotoxic profile of T cells[43,44]. Also, the phosphoprotein 1 (SPP1) signaling pathway, previously associated with immunosuppression and poor prognosis in lung cancer[45], showed decreased interactions, particularly between macrophages and other immune cells (AP-DCs, T cells, NKs, and B

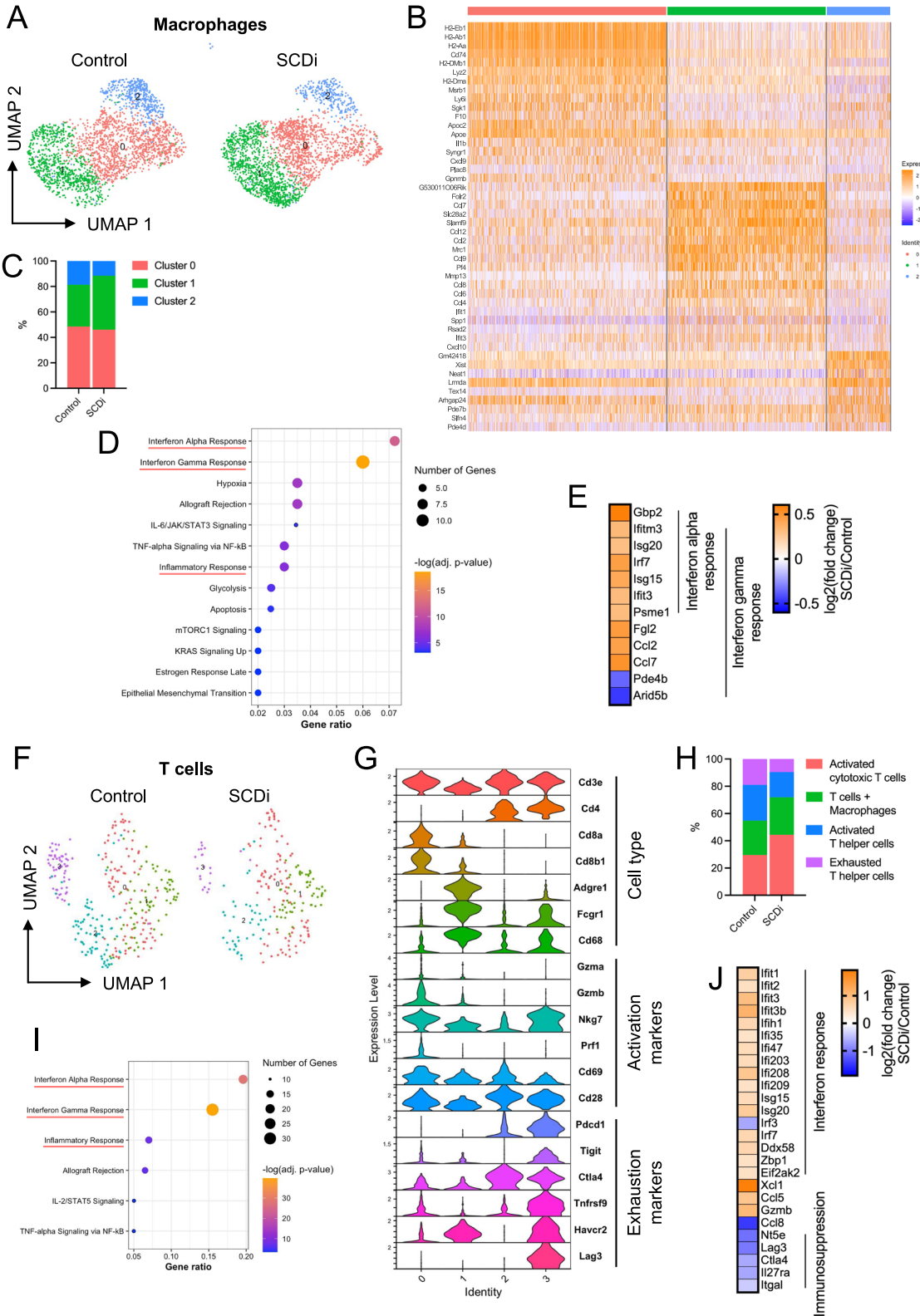

Fig. 4 | Inhibition of SCD enhances interferon signaling in macrophages and T cells and decreases T cell exhaustion in the TME. A UMAP of macrophages in control and SCDi-treated tumors. **B** Heatmap of the top 20 upregulated genes in the macrophage subclusters. **C** Histograms representing proportions of macrophage subpopulations in control and SCDi-treated tumors. **D** Pathway analysis (MSigDB) of the differentially expressed genes (DEGs) in macrophages (SCDi vs control). **E** Heatmap representing the DEGs belonging to the interferon alpha and gamma response pathways in macrophages (SCDi vs control). **F** UMAP of T cells in control and SCDi-treated tumors. **G** Violin plots showing the expression of cell type, activation, and exhaustion markers in the T cell subclusters. Cluster 0 represents activated cytotoxic T cells, cluster 1 represents T cells + macrophages, cluster 2 represents activated T helper cells, and cluster 3 represents exhausted T helper cells. **H** Histograms representing proportions of T cell subclusters in control and SCDi-treated tumors. **I** Pathway analysis (MSigDB) of the DEGs in T cells (SCDi vs control). **J** Heatmap representing a subset of relevant DEGs in T cells (SCDi vs control).

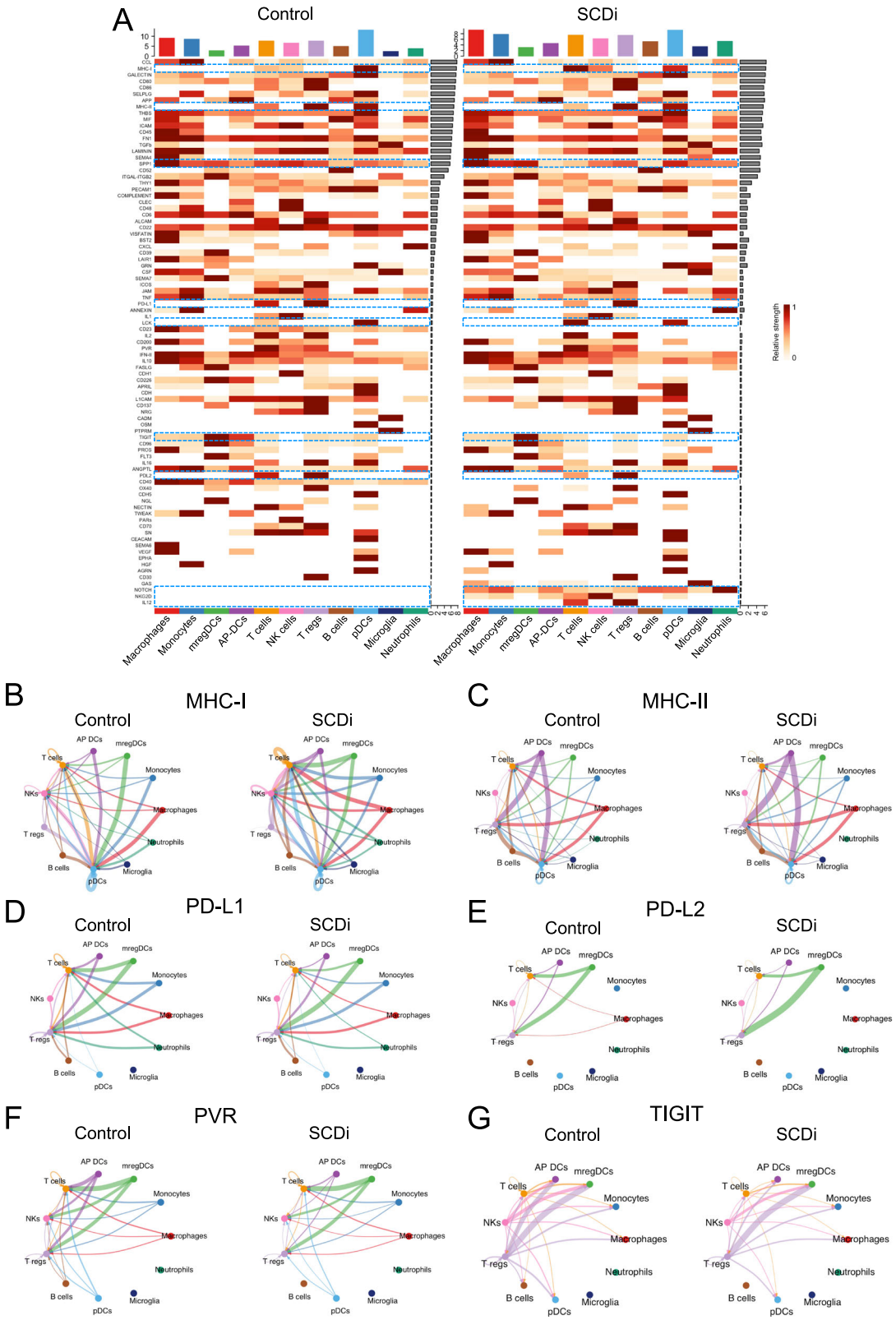

Fig. 5 | Interactions via PD-1:PD-L1/PD-L2 and PVR/TIGIT immunosuppressive axes are weakened in response to inhibition of SCD. A Overall signaling patterns between CellChat-curated pathways and cell clusters in control and SCDi-treated tumors. The relative strength reflects the sum of all normalized interactions in each pathway. Inferred **B** MHC-I, **C** MHC-II, **D** PD-L1, **E** PD-L2, **F** PVR, and **G** TIGIT signaling networks among the cell populations represented by the nodes in control and SCDi-treated tumors. The thickness of lines connecting two cell populations represents the interaction strength (i.e., thicker lines represent stronger interactions).

cells) in SCDi-treated tumors (Fig. S6G). Treatment with SCDi also resulted in stronger interactions via the LCK signaling pathway (Fig. S6H), which is crucial for T cell activation[46]. We also found stronger interactions via the Notch pathway, Nkg2d, and Il12 upon SCD inhibition (Fig. 5A). Together, these data support a higher activation status via MHC-I and LCK pathways and a diminished level of immunosuppression via PD-L1/PD-L2, and PVR/TIGIT in response to SCDi, likely contributing to an enhanced anti-tumor T cell response in the TME.

Discussion

Effective therapies for patients with BCBM are lacking. This study explored the therapeutic efficacy of a novel brain-penetrant SCDi on BCBM and the role of pharmacological inhibition of SCD on the TME. We characterized the transcriptome of the EO771 brain TME, generating a comprehensive cellular atlas that could be used by others.

Jin and co-authors showed high brain tropism of the TNBC cell lines MDA-MB-231 and HCC1806 in mouse xenografts[8]. In our study, these two cell lines and the brain-tropic cell line MDA-BR, showed the highest sensitivity to SCDi, in agreement with an increased dependency of BM on fatty acid metabolism[8,9]. The therapeutic efficacy of PARP inhibitors, currently being tested for the treatment of BCBM[47], is limited to BRCA-deficient tumors[25]. Additionally, high RAD51 expression predicted poor response to PARPi[48]. As a result, it was proposed that the combination of RAD51 and PARP inhibitors was effective in BRCA-wild-type breast cancer cells[26]. In line with the downregulation of RAD51 and impaired HDR following SCD inhibition in vitro and in vivo, we found that SCDi sensitized a BRCA-wild type mouse model of BCBM to PARPi, resulting in greater anti-tumor activity. These clinically relevant results support further testing of SCD and PARP inhibitors as a combination therapy for BCBM and other PARPi-resistant tumors.

Fatty acid metabolism reprogramming has been shown to affect the proliferation, differentiation, and activation of immune cells in the TME[49]. Consequently, a growing body of research has explored the role of fatty acid metabolism in immune cells to develop new anti-tumor therapeutic strategies. We report an increased DC activation upon SCD inhibition. Multiple mechanisms might explain this. For example, following DNA damage, tumor cells accumulate DNA in the cytosol that functions as an immunogenic danger signal, ultimately activating the expression of type I interferon-stimulated genes (ISGs)[50]. Moreover, damaged/dying tumor cells shed DNA that activates DCs via toll-like receptor 3 (TLR3), TLR9, and cGAS/STING[50,51]. Lastly, other molecules, known as damage-associated molecular patterns (DAMPs), released by damaged/dying cancer cells activate other TLRs (i.e., TLR2 and TLR4), ultimately leading to higher immune cell activation[39]. We also found higher interferon signaling in the TME of SCDi-treated tumors. Interferons are key components of immune cell activation[52]. They act on tumor cells to exert a direct anti-tumor effect, inducing apoptosis[53]. They can also regulate the activity of many immune cell types, leading to a balanced anti-tumor immune response. For example, they can activate DCs to enhance antigen presentation to T cells and recruit $CD4^+$ Th1 and $CD8^+$ T cells to the TME[54]. Also, interferons enhance macrophage activity by polarizing monocytes into mature pro-inflammatory anti-tumor M1 macrophages[53,55]. Moreover, interferons regulate the cytotoxic and anti-tumor activity of NK and T cells to exert a more effective anti-tumor immune response[56].

In line with heightened inflammatory responses in SCDi-treated tumor-bearing mice, we observed a shift in the balance of effector and immunosuppressive T cells in the TME. Previous studies reported that SCD inhibition was associated with an enhanced proliferation of $CD8^+$ T cells in various mouse tumor models[18], and with a greater T effector function in an LCMV infection model[15]. We found that SCDi-treated tumors were associated with reduced T cell exhaustion, diminished recruitment of Tregs, and dampened signaling through immunosuppressive pathways, such as the PD-L1/PD-L2 and the PVR/TIGIT axes. T cell exhaustion is a hypofunctional T cell state characterized by a decreased anti-tumor effect[57]. Tregs have an immunosuppressive role in inflammation and can suppress anti-tumor immunity[58]. The PD-L1/PD-L2 signaling pathway can inhibit the activation and effector function of T cells, ultimately driving tumor immune escape[59]. Similarly, the immunosuppressive PVR/TIGIT pathway is currently being investigated as a target for immunotherapy[44]. We believe this effect is likely a combination of intrinsic effects that SCDi has on T cell function and the impact of SCDi on antigen-presenting cells (i.e., DCs and macrophages) in the TME. Likely, the impact of SCDi on DNA damage and tumor cell viability is also a contributing factor. Overall, these data suggest that SCD inhibition is a potential strategy for turning "cold" immune-excluded tumors into "hot" immune-inflamed ones. Brain tumors are considered "cold" tumors, characterized by an immunosuppressive TME and a poor response to immunotherapy, partly due to the highly complex brain microenvironment[60,61]. The premise of developing a strategy that prompts an immune-inflamed TME and potentially bolsters immunotherapy is promising. As such, we speculate that combining SCDi with immune checkpoint inhibitors could be a strategy to treat BCBM that warrants further investigation. This is further supported by previous findings showing that SCD inhibition, or knockout, in mice potently enhanced the antitumor efficacy of anti-PD-1 immunotherapy in various mouse tumor models[18]. Additionally, considering the high therapeutic efficacy of the combination of SCDi with a PARPi in our immunodeficient BCBM mouse model, studying the effect of this combination, possibly with an immune checkpoint inhibitor, in a syngeneic immunocompetent mouse model of BCBM could be an interesting approach for future studies.

There are limitations to this study. First, the efficacy of SCDi was explored using one xenograft (MDA-BR) and one syngeneic (EO771) mouse model. Additionally, our BCBM model relied on direct injection of breast cancer cells into the brain of mice rather than spontaneous BM from intramammary or intravenous injections of HBC cells. This allowed us to directly assess the therapeutic efficacy of SCDi on established brain tumors, as this is the typical clinical scenario in patients diagnosed with BCBM. Also, the molecular mechanisms by which DCs show higher antigen-presenting ability and T cells show dampened exhaustion upon pharmacological inhibition of SCD remain to be elucidated. Moreover, whether the changes in the TME are due to a direct effect of SCD inhibition on immune cells or solely to the indirect effect of SCDi-induced cancer cell death remains an outstanding question. Finally, combining SCDi with PARPi in an immunocompetent mouse model, potentially with an immune checkpoint inhibitor, is a therapeutic strategy that warrants further investigation.

In conclusion, this study highlights the dual role of pharmacological inhibition of SCD in BCBM mouse models. In our immunodeficient BCBM mouse model, we show that SCDi has a direct immune-independent effect on cancer cells, triggering lipotoxicity and impairing DNA damage repair. In addition to that, SCDi promotes an anti-tumor immune response in the TME, as shown in our syngeneic BCBM mouse model. Our findings provide a rationale for combining SCDis with immunotherapy to treat these otherwise incurable tumors.

Methods

Cell lines

HBC cell lines MDA-MB-231, MCF7, HCC1806, MDA-MB-468, and BT474, and mouse mammary cancer cell line EO771 were purchased from American Type Culture Collection (ATCC; Manassas, VA, USA). Brain tropic MDA-MB-231-BR (MDA-BR) cells were kindly provided by Dr Patricia S. Steeg (National Cancer Institute, Bethesda, MD). All cells were cultured at 37 °C in a 5% CO_2 humidified incubator. The culture medium for MDA-MB-231, MCF7, MDA-MB-468, and MDA-BR cells was Dulbecco's Modified Essential Medium (DMEM, Corning) supplemented with penicillin (100 units/ml), streptomycin (100 mg/ml) (P/S) (Corning) and 10% fetal bovine serum (FBS; Atlanta Biologics). The culture medium for HCC1806 and BT474 cells was Roswell Park Memorial Institute (RPMI, ATCC) supplemented with P/S (Corning) and 10% FBS (Atlanta Biologics). The culture medium for EO771 cells was DMEM supplemented with P/S (Corning), 10% FBS (Atlanta Biologics), and 20 mM HEPES (Thermo Fisher Scientific).

In vivo mouse models

Animal experiments were approved by the Massachusetts General Hospital Subcommittee on Research Animal Care or by the University of California, Los Angeles Animal Research Committee. For orthotopic mouse models, 6–8 week female athymic nude mice were injected into the mammary fat pad with 1×10^6 MDA-BR cells in a 100 µl mixture composed of Matrigel (50 µl; BD Matrigel 10 mg/ml, BD Biosciences) and PBS (50 µl). For intracranial mouse models, 6–8-weeks-old female mice were intracranially injected with 5×10^4 MDA-BR cells (athymic nude mice) or 5×10^2 EO771 expressing Luc-GFP (C57BL/6J) in PBS (2 µl) as previously described in ref. 13. The number of mice used in each study is reported in the corresponding figure legends. Our study exclusively examined female mice because the disease modeled is only relevant in females. For in vivo studies, YTX-7739 (100 µl) was administered by intraperitoneal injections, daily. Niraparib (100 µl) was administered by oral gavage, daily. Control groups were administered with 100 µl of vehicle (0.5% methylcellulose + 0.2% Tween80 in saline solution).

Reagents/test inhibitors

For in vitro studies, YTX-7739 (SCDi), Niraparib (MK-4827, Selleckchem), Z-VAD-FMK (Selleckchem), 4-Phenylbutyric acid (4-PBA, MedChemExpress), and GSK2606414 (Millipore Sigma) were dissolved in DMSO. For in vivo studies, YTX-7739 was dissolved by sonication (2-3 min), heating (3 min at 60 °C), and vortexing in 0.5% methylcellulose + 0.2% Tween80 in sterile saline solution. Niraparib was prepared as per the manufacturer's instructions. Bovine serum albumin (BSA)-conjugated oleate (18:1) monounsaturated fatty acid complex was obtained from Cayman Chemical.

^{13}C-glucose labeling experiments

HBC cells ($1–4 \times 10^5$ per well of a 12-well plate) were plated in 3 replicates and treated with DMSO or SCDi (0.1 µM or 1 µM) in serum-free glucose-free media, supplemented with 2.25 g/L of unlabeled D-glucose (Millipore Sigma) and 2.25 g/l of $^{13}C_6$-glucose (Cambridge Isotope Laboratories). After 24 h and 48 h, cells were collected and counted using the Cellometer K2 Cell Counter (Nexcelom). Then, $1–3 \times 10^5$ cells were resuspended in 3 M methanolic guanidine HCl and immediately transferred to glass tubes for derivatization. Samples were prepared alongside internal standard curve samples made up of FAMEs (Nu-Chek Prep). Isotopomer spectral analysis (ISA) was conducted using an Agilent 5975 C mass spectrometer coupled to a 7890 Gas Chromatograph, as previously described in ref. 62. Data were normalized by total cell count.

Shotgun lipidomics

MDA-BR cells (4×10^5 per well of a 6-well plate) were plated in 4 replicates and treated with DMSO or SCDi (1 µM) in serum-free media. After 48 h, cells were then collected and counted using the Cellometer K2 Cell Counter (Nexcelom). Shotgun lipidomic analysis was performed as previously described in ref. 13. Briefly, after the addition of internal standards consisting of 70 lipid standards across 17 subclasses (AB Sciex, 5040156; Avanti, 330827; Avanti, 330830; Avanti, 330828; and Avanti, 791642) and two successive extractions, organic layers were vacuum-dried in a Thermo Fisher Scientific SpeedVac SPD300DDA machine, at 35 °C for 45 min with a total run time of 90 min. Samples were then resuspended in methanol/dichloromethane (1:1 ratio) with 10 mM ammonium acetate and transferred to robovials (Thermo Fisher Scientific, 10800107) for subsequent lipidomic analysis. Samples were then analyzed by direct infusion using the Sciex 5500 with differential mobility device (DMS) (comparable to the Sciex Lipidyzer platform) for quantitative measurement of 1450 lipid species belonging to 17 subclasses. The DMS was tuned with Equi-SPLASH LIPIDOMIX (Avanti, 330731). Quantitative values of lipid species were normalized to cell counts. Heatmaps and Principal Component Analysis (PCA) plots were generated using Clustvis (https://biit.cs.ut.ee/clustvis/). The color scale on heatmaps refers to the row Z score. Nipals PCA was used to calculate principal components (PCs) on PCA. X and Y axes show PC1 and PC2, which refer to the percentage of the total variance, respectively.

Lentiviral vectors and transduction

CSCW-GLuc-IRES-GFP lentiviral vector expressing Gaussia Luciferase (GLuc) and green fluorescent protein (GFP) was used. Cells ($2–4 \times 10^5$) were seeded in a 6-well plate to transduce cancer cell lines. Polybrene (10 µg/ml; Millipore Sigma) and 10–30 µl of lentivirus were added to each well when cells were attached. Cells were spun at 1800 rpm at 4 °C for 1.5 h and incubated at 37 °C. After 12-14 h, the medium was replaced with fresh medium. GFP-positive cells were then selected by fluorescent activated cell sorting (FACS).

In vitro assays

Cell viability assays were performed using CellTiter-Glo 2.0 (Promega). Apoptosis was measured using Caspase-Glo 3/7 (Promega). Early apoptosis and late apoptosis/necrosis were measured using Alexa Fluor 488 Annexin V/Dead Cell Apoptosis Kit (Thermo Fisher Scientific). These reagents were used as indicated by the manufacturer. All experiments were performed in triplicate.

Protein extraction and western blotting

Radioimmunoprecipitation assay buffer (RIPA) buffer (Thermo Fisher Scientific) supplemented with protease and phosphatase inhibitors (Thermo Fisher Scientific) was used to lyse cells and extract proteins, as recommended by the manufacturer. Protein concentration was calculated using the Pierce BCA Protein Assay Kit (Thermo Fisher Scientific), following manufacturer's instructions, and 10-30 µg of protein were loaded and resolved on either a 10% or 4–12% Bolt Bis-Tris gel (Thermo Fisher Scientific), transferred to a nitrocellulose membrane (Bio-Rad), and then incubated with the indicated antibodies. Proteins were then detected with SuperSignal West Pico Chemiluminescent Substrate (Thermo Fisher Scientific). The following antibodies were used: PARP (CST #9532), phospho-eIF2α (CST #3597), ATF-4 (CST #11815), Phospho-Histone H2A.X (γ-H2AX) (CST #9718), anti-rabbit IgG, HRP-linked (CST #7074) and Anti-mouse IgG, HRP-linked (CST #7076), GAPDH (Santa Cruz #sc-47724), beta actin (Abcam #ab227387), Rad51 (BIOSS Antibodies #BSM-51402M). All experiments were performed in triplicate.

RNA extraction and quantitative PCR

RNA was extracted using the Quick-RNA MiniPrep kit (Zymo Research). RT-PCR was performed using the High-Capacity cDNA Reverse Transcription Kit (Thermo Fisher Scientific). qPCR was performed using the PowerUP SYBR Green Master Mix (Thermo Fisher Scientific) using Qthe uantStudio 3 System. All reagents were used as recommended by the manufacturers. Relative mRNA expression was calculated using the $2^{-\Delta\Delta CT}$ method. Beta-actin or HPRT1 was used as ha ousekeeping gene. Primer sequences are reported in Table S1. All experiments were performed in triplicate.

Bioluminescence BLRR assay to monitor DNA damage repair

The bioluminescent repair reporter (BLRR) system was used to track DNA damage repair, as previously described in ref. 21. Briefly, cells were sequentially transduced to express BLRR, trGluc, and I-SceI. To detect BLRR activity in vitro, cells were plated in a 96-well plate and treated with DMSO or SCDi (0.1 µM and 1 µM). On days 1, 2, 3, and 4 post-treatment, 25 µl of the conditioned medium was collected and transferred into a white 96-well plate to measure luminescence using a multimode reader (Biotek). Coelentrazine (20 µM; Nanolight) and Vargulin (5 ng/ml; Nanolight) were used to detect Gaussia luciferase (Gluc; HDR) and Vargula luciferase (Vluc; NHEJ) activities, respectively. All luminescence results were normalized to cell viability measured using CellTiter-Glo2.0. These experiments were performed in triplicate. To detect BLRR activity in vivo, 1×10^6 MDA-BR cells were injected into the mammary fat pad of 6–8-week-old female athymic nude mice. Mice were treated with vehicle/SCDi for 21 days, as described. On the day of euthanasia, blood was collected into a K_2-EDTA blood collection tube and spun at 2000 rcf for 15 min. Twenty-five µl of

plasma was transferred into a white 96-well plate (in three replicates) to measure luminescence, as described above.

Tissue digestion

Neural Tissue Dissociation Kit (P) (Miltenyi Biotec) was used to digest the brains into a single cell suspension, according to the manufacturer's instructions. Myelin was removed using anti-myelin beads (Miltenyi Biotec), following the manufacturer's instructions. The final single cell suspension was resuspended in 1× PBS w/o calcium and magnesium, supplemented with 2 mM EDTA (Thermo Fisher Scientific) and 0.5% BSA (Millipore Sigma), before cell staining and fluorescent-activated cell sorting (FACS).

Single-cell RNA sequencing

For scRNAseq, three mice per experimental group were pooled into 1 sample prior to FACS-sorting to account for inter-animal variability. Each brain pool was sorted into 2 cell populations: tumor cells ($DAPI^-/CD45^-/GFP^+$) and immune cells ($DAPI^-/CD45^+/GFP^-$). Within 30 min after sorting, 3' scRNA-seq libraries were generated using a 10X Genomics Chromium controller. Libraries were then sequenced on a NovaSeq 6000 platform using a NovaSeq S2 flow cell (Illumina). Data analysis was performed in R Studio (v1.3.1073) using Seurat (v4.1.1). Cells with less than 1000 detected genes, UMI numbers <300, or with >2% mitochondrial-derived UMI counts were excluded from the analysis. Raw Fastq data were processed using CellRanger v3.0.2. Cell clusters were identified with the FindClusters function and visualized on UMAP plots using the top 30 dimensions for the analysis. Cell types were annotated based on the corresponding literature. Differentially expressed genes (DEGs) of cell subgroups were recognized by the FindAllMarker function, using $|\log FC| = 0.3$ and adjusted p-value < 0.05 as the cut-off criteria. Pathway on DEGs was performed using enrichr, KEGG_2019_Mouse and HDSigDB_Mouse_2021 packages. The analysis of cell-cell communication networks was performed by integrating all samples and visualized using the netVisual_circle and netVisual_heatmap functions. The centrality score was computed using the netAnalysis_computeCentrality function, while the relative contribution of each ligand-receptor pair was visualized using the netAnalysis_signalingRole_heatmap, netVisual_bubble, and netVisual_chord_gene functions. Signals contributing the most to outgoing or incoming signaling were identified by the netAnalysis_signalingRole_heatmap function.

Bone marrow-derived dendritic cell culture

To generate type I conventional dendritic cells (cDC1s) in vitro, bone marrow progenitors from 6 to 10-weeks old C57BL/6 mice were resuspended at 1.5×10^7 cells in 10 ml of DC medium (RPMI 1640, 1% penicillin-streptomycin, 10% FBS, 1× Glutamax, 200 mM sodium pyruvate, 25 mM HEPES, 1% MEM-NEAA, 0.5% sodium bicarbonate, 0.01% 55 mM 2-mercaptoethanol supplemented with 200 ng/ml FLT3-L and 5 ng/ml GM-CSF), and seeded in 10 cm non-TC treated culture dishes and incubated at 37 °C, 5% CO_2. On day 5, 5 ml of fresh media were added to the cells. On day 9, the media was replaced, and cells were used for experiments on day 15.

Collection of EO771 conditioned medium and treatment of cDC1s

To generate EO771 conditioned medium (CM), EO771 cells were seeded at a density of 1.5×10^5 cells per well of a 6-well plate in complete medium. The next day, the medium was replaced with DMEM/F12 + 1% penicillin-streptomycin supplemented with either 0.1% DMSO (Untr EO771 CM) or 1 μM SCDi (SCDi EO771 CM). After 48 h of treatment, the medium was collected and centrifuged at 300rcf for 5 min to remove cell debris. For CM treatment, 5×10^5 cDC1s were seeded in triplicate in a non-TC-treated 24-well plate in 250 μl complete medium + 250 μl EO771 CM. After 16 h and 24 h, cDC1s were collected and analyzed by qPCR and flow cytometry, respectively. For the antigen presentation assay, cDC1s were exposed to EO771 CM for 24 h, and then pulsed with 1 μM $OVA_{257\text{-}264}$ (Invivogen) for 1 h. Cells were then washed three times with PBS and stained for flow cytometry analysis.

Flow cytometry

Non-specific binding was blocked by incubating cells with TruStain FcX (anti-mouse Cd16/32, BioLegend) for 5–10 min. Cells were then stained with the antibodies for 30 min on ice in the dark. Cells were then washed with PBS + 2%FBS + 2 mM EDTA (FACS buffer), centrifuged at 300 rcf for 5 min, and resuspended in FACS buffer. DAPI was added to the single cell suspension at a final concentration of 1 μg/ml to stain dead cells. Cells were then sorted using a BD FACSAria II cell sorter. Cells for scRNAseq were sorted into 100% FBS. The following antibodies were purchased from BioLegend: BV785-anti-CD45, BV711-anti-CD11c, ACP/Cy7-anti-I-A/I-E, BV650-anti-XCR1, AF647-anti-H-2Kb/H-2Db, PE/Cy7-anti-CD40, PE/Dazzle594-anti-CD80, BV421-anti-CD86, APC-anti-H-2Kb bound to SIINFEKL.

Statistics and reproducibility

Statistical analysis was performed using Prism 10 (GraphPad Software). All measurements were taken from distinct samples. To verify differences between two groups, the Student's t-test, when data were normally distributed, and the Mann-Whitney test when data were not normally distributed, were used. To verify the difference between more than two groups, one-way analysis of variance (ANOVA) followed by Tukey's multiple comparisons test when data were normally distributed and the Kruskal–Wallis test followed by Dunn's multiple comparisons test when data were not normally distributed were used. Normality distribution was tested using the Shapiro–Wilk test. Survival curves were generated and analyzed using a log-rank test (Mantel–Cox). The level of significance was fixed as $p < 0.05$. Graphs were generated using GraphPad Prism 10 or R Studio.

Reporting summary

Further information on research design is available in the Nature Portfolio Reporting Summary linked to this article.

Data availability

The numerical source data for the graphs presented in the main figures are available in Supplementary Data 1. The uncropped and unedited blot images are available in Supplementary Materials. The scRNAseq datasets generated in the current study are available at NCBI GEO with accession number GSE292006.

Received: 16 August 2024; Accepted: 21 March 2025;
Published online: 04 April 2025

References

1. Achrol, A. S. et al. Brain metastases. *Nat. Rev. Dis. Primers* **5**, 5 (2019).
2. Nayak, L., Lee, E. Q. & Wen, P. Y. Epidemiology of brain metastases. *Curr. Oncol. Rep.* **14**, 48–54 (2012).
3. Sperduto, P. W. et al. Diagnosis-specific prognostic factors, indexes, and treatment outcomes for patients with newly diagnosed brain metastases: a multi-institutional analysis of 4,259 patients. *Int J. Radiat. Oncol. Biol. Phys.* **77**, 655–661 (2010).
4. Berghoff, A. S. et al. Descriptive statistical analysis of a real life cohort of 2419 patients with brain metastases of solid cancers. *ESMO Open* **1**, e000024 (2016).
5. Müller, S. et al. Brain metastases from colorectal cancer: a systematic review of the literature and meta-analysis to establish a guideline for daily treatment. *Cancers***13**, 900 (2021).
6. Kolsi, F. et al. Delayed brain metastasis from renal cell carcinoma. *Urol. Case Rep.* **22**, 54–56 (2018).
7. Hall, W. A., Djalilian, H. R., Nussbaum, E. S. & Cho, K. H. Long-term survival with metastatic cancer to the brain. *Med. Oncol.* **17**, 279–286 (2000).

8. Jin, X. et al. A metastasis map of human cancer cell lines. *Nature* **588**, 331–336 (2020).
9. Ferraro, G. B. et al. Fatty acid synthesis is required for breast cancer brain metastasis. *Nat. Cancer* **2**, 414–428 (2021).
10. Scott, J. S., Nassar, Z. D., Swinnen, J. V. & Butler, L. M. Monounsaturated fatty acids: key regulators of cell viability and intracellular signaling in cancer. *Mol. Cancer Res.* **20**, 1354–1364 (2022).
11. Tardiff, D. F. et al. Non-clinical Pharmacology of YTX-7739: a clinical stage stearoyl-CoA desaturase inhibitor being developed for Parkinson's disease. *Mol. Neurobiol.* **59**, 2171–2189 (2022).
12. Pinkham, K. et al. Stearoyl CoA desaturase is essential for regulation of endoplasmic reticulum homeostasis and tumor growth in glioblastoma cancer stem cells. *Stem Cell Rep.* **12**, 712–727 (2019).
13. Eyme, K. M. et al. Targeting de novo lipid synthesis induces lipotoxicity and impairs DNA damage repair in glioblastoma mouse models. *Sci. Transl. Med.* **15**, eabq6288 (2023).
14. Xiao, Y., Yang, Y., Xiong, H. & Dong, G. The implications of FASN in immune cell biology and related diseases. *Cell Death Dis.* **15**, 1–12 (2024).
15. Lin, Y. et al. Scd-1 deficiency promotes the differentiation of CD8+ T effector. *Front Cell Infect. Microbiol.* **14**, 1325390 (2024).
16. York, A. G. et al. IL-10 constrains sphingolipid metabolism to limit inflammation. *Nature* **627**, 628–635 (2024).
17. Zhao, G. et al. Ovarian cancer cell fate regulation by the dynamics between saturated and unsaturated fatty acids. *Proc. Natl. Acad. Sci. USA* **119**, e2203480119 (2022).
18. Katoh, Y. et al. Inhibition of stearoyl-CoA desaturase 1 (SCD1) enhances the antitumor T cell response through regulating β-catenin signaling in cancer cells and ER stress in T cells and synergizes with anti-PD-1 antibody. *J. Immunother. Cancer* **10**, e004616 (2022).
19. Piccolis, M. et al. Probing the global cellular responses to lipotoxicity caused by saturated fatty acids. *Mol. Cell* **74**, 32–44.e8 (2019).
20. Ribeiro, C. F. et al. Blocking lipid synthesis induces DNA damage in prostate cancer and increases cell death caused by PARP inhibition. *Sci. Signal.* **17**, eadh1922 (2024).
21. Chien, J. C. Y. et al. A multiplexed bioluminescent reporter for sensitive and non-invasive tracking of DNA double strand break repair dynamics in vitro and in vivo. *Nucleic Acids Res.* **48**, E100 (2020).
22. Sun, C. et al. BRD4 inhibition is synthetic lethal with PARP inhibitors through the induction of homologous recombination deficiency. *Cancer Cell* **33**, 401–416.e8 (2018).
23. Bryant, H. E. et al. Specific killing of BRCA2-deficient tumours with inhibitors of poly(ADP-ribose) polymerase. *Nature* **434**, 913–917 (2005).
24. Ledermann, J. A. et al. Overall survival in patients with platinum-sensitive recurrent serous ovarian cancer receiving olaparib maintenance monotherapy: an updated analysis from a randomised, placebo-controlled, double-blind, phase 2 trial. *Lancet Oncol.* **17**, 1579–1589 (2016).
25. Li, H. et al. PARP inhibitor resistance: the underlying mechanisms and clinical implications. *Mol. Cancer* **19**, 107 (2020).
26. Sambade, M. J. et al. Efficacy and pharmacodynamics of niraparib in BRCA-mutant and wild-type intracranial triple-negative breast cancer murine models. *Neurooncol. Adv.* **1**, vdz005 (2019).
27. Garber, H. R. et al. Incidence and impact of brain metastasis in patients with hereditary BRCA1 or BRCA2 mutated invasive breast cancer. *NPJ Breast Cancer* **8**, 1–8 (2022).
28. Meisen, W. H. et al. Changes in BAI1 and nestin expression are prognostic indicators for survival and metastases in breast cancer and provide opportunities for dual targeted therapies. *Mol. Cancer Ther.* **14**, 307–314 (2015).
29. Russell, L. et al. PTEN expression by an oncolytic herpesvirus directs T-cell mediated tumor clearance. *Nat. Commun.* **9**, 5006 (2018).
30. Thies, K. A. et al. Stromal platelet-derived growth factor receptor-β signaling promotes breast cancer metastasis in the brain. *Cancer Res.* **81**, 606–618 (2021).
31. Sun, Q., et al. SCD1 is the critical signaling hub to mediate metabolic diseases: mechanism and the development of its inhibitors. *Biomed. Pharmacother.* **170**, 115586 (2024).
32. Sen, U., Coleman, C. & Sen, T. Stearoyl coenzyme A desaturase-1: multitasker in cancer, metabolism, and ferroptosis. *Trends Cancer* **9**, 480–489 (2023).
33. Wang, Y. et al. Centrosome-associated regulators of the G2/M checkpoint as targets for cancer therapy. *Mol. Cancer* **8**, 8 (2009).
34. Cam, H. & Dynlacht, B. D. Emerging roles for E2F: beyond the G1/S transition and DNA replication. *Cancer Cell* **3**, 311–316 (2003).
35. Derynck, R., Turley, S. J. & Akhurst, R. J. TGFβ biology in cancer progression and immunotherapy. *Nat. Rev. Clin. Oncol.* **18**, 9–34 (2021).
36. Li, J. et al. Lipid desaturation is a metabolic marker and therapeutic target of ovarian cancer stem cells. *Cell Stem Cell* **20**, 303–314.e5 (2017).
37. Murphy, T. L. & Murphy, K. M. Dendritic cells in cancer immunology. *Cell Mol. Immunol.* **19**, 3–13 (2022).
38. Maier, B. et al. A conserved dendritic-cell regulatory program limits antitumour immunity. *Nature* **580**, 257–262 (2020).
39. Jang, G. -Y. et al. Interactions between tumor-derived proteins and Toll-like receptors. *Exp. Mol. Med.* **52**, 1926–1935 (2020).
40. Nalio Ramos, R. et al. Tissue-resident FOLR2+ macrophages associate with CD8+ T cell infiltration in human breast cancer. *Cell* **185**, 1189–1207.e25 (2022).
41. Bödder, J. et al. Harnessing the cDC1-NK cross-talk in the tumor microenvironment to battle cancer. *Front. Immunol.* **11**, 631713 (2021).
42. Halvorsen, E. C. et al. Maraviroc decreases CCL8-mediated migration of CCR5+ regulatory T cells and reduces metastatic tumor growth in the lungs. *Oncoimmunology* **5**, e1150398 (2016).
43. Gorvel, L. & Olive, D. Targeting the "PVR–TIGIT axis" with immune checkpoint therapies. *F1000Res* **9**, F1000 Faculty Rev-354 (2020).
44. Chiang, E. Y. & Mellman, I. TIGIT-CD226-PVR axis: advancing immune checkpoint blockade for cancer immunotherapy. *J. Immunother. Cancer* **10**, e004711 (2022).
45. Matsubara, E. et al. SPP1 Derived from macrophages is associated with a worse clinical course and chemo-resistance in lung adenocarcinoma. *Cancers***14**, 4374 (2022).
46. Stirnweiss, A. et al. T cell activation results in conformational changes in the Src family kinase Lck to induce its activation. *Sci. Signal.* **6**, ra13–ra13 (2013).
47. Bailleux, C., Eberst, L. & Bachelot, T. Treatment strategies for breast cancer brain metastases. *Br. J. Cancer* https://doi.org/10.1038/s41416-020-01175-y (2020).
48. Cruz, C. et al. RAD51 foci as a functional biomarker of homologous recombination repair and PARP inhibitor resistance in germline BRCA-mutated breast cancer. *Ann. Oncol.* **29**, 1203–1210 (2018).
49. Zhang, S., Lv, K., Liu, Z., Zhao, R. & Li, F. Fatty acid metabolism of immune cells: a new target of tumour immunotherapy. *Cell Death Discov.* **10**, 1–12 (2024).
50. Lopez-Pelaez, M. et al. Targeting DNA damage response components induces enhanced STING-dependent type-I IFN response in ATM deficient cancer cells and drives dendritic cell activation. *Oncoimmunology* **11**, 2117321 (2022).
51. Kang, T. H. et al. TLR9 acts as a sensor for tumor-released DNA to modulate anti-tumor immunity after chemotherapy. *J. Immunother. Cancer* **7**, 260 (2019).
52. Fenton, S. E., Saleiro, D. & Platanias, L. C. Type I and II interferons in the anti-tumor immune response. *Cancers***13**, 1037 (2021).

53. Parker, B. S., Rautela, J. & Hertzog, P. J. Antitumour actions of interferons: implications for cancer therapy. *Nat. Rev. Cancer* **16**, 131–144 (2016).
54. Schiavoni, G., Mattei, F. & Gabriele, L. Type I interferons as stimulators of DC-mediated cross-priming: impact on anti-tumor response. *Front. Immunol.* **4**, 483 (2013).
55. Müller, E. et al. Both type I and type II interferons can activate antitumor M1 macrophages when combined with TLR stimulation. *Front. Immunol.* **9**, 2520 (2018).
56. Siveen, K. S. & Kuttan, G. Role of macrophages in tumour progression. *Immunol. Lett.* **123**, 97–102 (2009).
57. Chow, A., Perica, K., Klebanoff, C. A. & Wolchok, J. D. Clinical implications of T cell exhaustion for cancer immunotherapy. *Nat. Rev. Clin. Oncol.* **19**, 775–790 (2022).
58. Togashi, Y., Shitara, K. & Nishikawa, H. Regulatory T cells in cancer immunosuppression—implications for anticancer therapy. *Nat. Rev. Clin. Oncol.* **16**, 356–371 (2019).
59. Jiang, X. et al. Role of the tumor microenvironment in PD-L1/PD-1-mediated tumor immune escape. *Mol. Cancer* **18**, 10 (2019).
60. Sevenich, L. et al. Analysis of tumour- and stroma-supplied proteolytic networks reveals a brain-metastasis-promoting role for cathepsin S. *Nat. Cell Biol.* **16**, 876–888 (2014).
61. Brown, C. E. et al. The future of cancer immunotherapy for brain tumors: a collaborative workshop. *J. Transl. Med.* **20**, 236 (2022).
62. Williams, K. J. et al. An essential requirement for the SCAP/SREBP signaling axis to protect cancer cells from lipotoxicity. *Cancer Res.* **73**, 2850–2862 (2013).

Acknowledgements

This work was supported by NIH/NINDS R01 NS113822 (C.E.B.), DoD Peer Reviewed Cancer Research CA191075 (C.E.B.), NIH/NCI P50 CA165962 SPORE in Brain Tumor Research subaward (C.E.B.), and NIH/NINDS R01 NS121319 (S.J.B.). Alessandro Sammarco was supported by an American–Italian Cancer Foundation Postdoctoral Research Fellowship. Katharina M. Eyme was supported by a German Academic Exchange Service (DAAD) scholarship. We are grateful to Yumanity Therapeutics for kindly providing YTX-7739. We would like to thank the Flow Cytometry Core at UCLA and the Applied Genomics, Computational & Translational Core at Cedars-Sinai Medical Center. We would like to thank Christopher Tse, David Nathanson, and Semer Maksoud for their help and Xandra Breakefield for her support. Graphics were created with Biorender (Biorender.com).

Author contributions

Conceptualization: A.S., S.J.B., and C.E.B. Methodology: A.S., S.J.B., and C.E.B. Validation: A.S., G.G., K.M.E., K.J.W., S.J.B., and C.E.B. Formal analysis: A.S., G.G., and B.S. Investigation: A.S., K.M.E., K.K., Y.Q., J.E.H., K.J.W., C.C., H.M., and V.Z. Resources: K.J.W., S.J.B., and C.E.B. Data Curation: A.S. and G.G. Writing original draft: A.S., S.J.B., and C.E.B. Writing—review and editing: G.G., K.M.E., K.K., Y.Q., J.E.H, K.J.W., B.S., C.C., H.M., and V.Z. Visualization: A.S. and G.G. Supervision: S.J.B. and C.E.B. Project administration: S.J.B. and C.E.B. Funding acquisition: S.J.B. and C.E.B.

Competing interests

C.E.B. received in-kind support from Yumanity Therapeutics. K.J.W. serves as a consultant for Verso Biosciences Inc.

Additional information

Supplementary information The online version contains supplementary material available at https://doi.org/10.1038/s42003-025-07977-1.

Correspondence and requests for materials should be addressed to Alessandro Sammarco or Christian E. Badr.

Peer review information *Communications Biology* thanks Markus Siegelin, Mara De Martino, and the other, anonymous, reviewer for their contribution to the peer review of this work. Primary Handling Editors: Joanna Hester and Mengtan Xing.